

Localizing quasi-periodic pulsations in hard X-ray, microwave and $\text{Ly}\alpha$ emissions of an X6.4 Flare

Dong Li^{1,2}, Zhenxiang Hong^{3,1}, Zhenyong Hou⁴, and Yang Su¹

¹*Key Laboratory of Dark Matter and Space Astronomy, Purple Mountain Observatory, CAS, Nanjing 210023, PR China*

²*Yunnan Key Laboratory of the Solar physics and Space Science, Kunming 650216, PR China*

³*Zhejiang International Studies University, Hangzhou, 310023, PR China*

⁴*School of Earth and Space Sciences, Peking University, Beijing 100871, PR China*

ABSTRACT

We report the simultaneous observations of quasi-periodic pulsations (QPPs) in wavelengths of hard X-ray (HXR), microwave, $\text{Ly}\alpha$, and ultraviolet (UV) emissions during the impulsive phase of an X6.4 flare on 2024 February 22 (SOL2024-02-22T22:08). The X6.4 flare shows three repetitive and successive pulsations in HXR and microwave wavebands, and they have an extremely-large modulation depth. The onset of flare QPPs is almost simultaneous with the start of magnetic cancellation between positive and negative fields. The wavelet power spectra suggest the presence of double periods, which are centered at ~ 200 s and ~ 95 s, respectively. The long-period QPP can also be detected in $\text{Ly}\alpha$ and UV wavebands at the flare area, and it could be observed in the adjacent sunspot. Our observations indicate that the flare QPPs are most likely triggered by accelerated electrons that are associated with periodic magnetic reconnections. The long period at ~ 200 s is probably modulated by the slow magnetoacoustic wave originating from the neighboring sunspot, while the short period at ~ 95 s could be regarded as its second harmonic mode.

Subject headings: Solar flares — Solar oscillations — Solar X-ray emission — Solar radio emission — Solar UV emission — Sunspots

1. Introduction

Quasi-periodic pulsations (QPPs) are frequently detected in the time series of solar flares, which are highly variable modulations to the flare radiation, and could be applied to diagnose the plasma fluctuations in the solar atmosphere (e.g., Kupriyanova et al. 2020; Zimovets et al. 2021a, references therein). The key feature of flare QPPs is repeatability, successiveness, and impulsiveness, which

Correspondence should be sent to: lidong@pmo.ac.cn

may play a crucial role in diagnosing the intermittent and impulsive energy-releasing process on the Sun (Inglis et al. 2023). A classic QPP event usually exhibits at least three successive pulsations in the time series, there is no reason to discuss the QPP feature if it shows just one or two pulsations, because this might be a random occurrence (e.g., Nakariakov et al. 2019). The flare QPPs are often composed by a group of nonstationary pulsations, termed as “nonstationary QPPs”, and the pulsation profile of this type is anharmonic and irregular (cf. Nakariakov et al. 2019). The flare QPP was first discovered by Parks & Winckler (1969) in the X-ray channel. After then, they have been observed in nearly all the electromagnetic wavebands, ranging from radio/microwave emissions, through white light, ultraviolet (UV), and extreme ultraviolet (EUV) wavelengths to soft/hard X-rays (SXR/HXR) and even to γ -rays (e.g., Nakariakov et al. 2010; Dennis et al. 2017; Nakariakov et al. 2018; Shen et al. 2022; Li et al. 2020a, 2022; Mehta et al. 2023; Motyk et al. 2023; Yu et al. 2024; Zhou et al. 2024). The flare QPPs were also seen in the Ly α emission (Milligan et al. 2017; Li et al. 2021; Lu et al. 2021). The quasi-periods of flare QPPs were observed in a wide range of timescales of minutes, seconds, or even milliseconds (e.g., Sych et al. 2009; Tan et al. 2010; Kumar et al. 2015; Karlický & Rybák 2020; Xu et al. 2023; Zhao et al. 2023; Millar et al. 2024). It seems that the detected period is highly associated with the observed waveband or the used instrument. Moreover, double or even multiple periods were simultaneously observed in the time series of the same flare, which could be explained as the fundamental and second or multiple harmonics (Inglis & Nakariakov 2009; Li 2022). The QPPs feature could also be found in the circular-ribbon flare, and this type of flare often occurs in a complicated magnetic structure associated with a fan-spine topology (cf. Török et al. 2009; Zhang 2024), resulting in various kinds of flare QPPs (e.g., Kashapova et al. 2020; Ning et al. 2022; Altyntsev et al. 2022).

Although the flare QPPs have been discovered more than fifty years (see, Parks & Winckler 1969), it is still in debate which generation mechanism should be responsible for triggering a specific QPP event, mainly because that the current observational data could not provide sufficient information to distinguish various mechanisms (e.g., Inglis et al. 2023). Assuming the presence of magnetohydrodynamic (MHD) waves and periodic magnetic reconnection on the Sun, more than fifteen types of mechanisms or models are proposed to interpret the flare QPPs (see Zimovets et al. 2021a, for a recent review). They could be regarded as a type of MHD wave, such as the slow-mode wave, the kink-mode wave, or the sausage-mode wave (see Li et al. 2020; Nakariakov et al. 2021; Wang et al. 2021, for reviews). This mechanism can be used to explain those flare QPPs that are strongly associated with magnetic loops and current sheets (Zimovets et al. 2021a). The flare QPPs could be driven by the repetitive regime of magnetic reconnection, which would periodically accelerate non-thermal ions and electrons (Thurgood et al. 2017; Karampelas et al. 2022; Corchado Albelo et al. 2024). The quasi-periodic reconnection may be spontaneous such as the self-oscillatory process (McLaughlin et al. 2009) and the magnetic tuning fork model (Takasao & Shibata 2016), or might be triggered by an external wave (Kumar et al. 2016; Nakariakov et al. 2018; Li & Chen 2022). These models well explain those QPPs seen in HXR and microwave emissions during the flare impulsive phase (e.g., Yuan et al. 2019; Clarke et al. 2021; Luo et al. 2022; Li et al. 2022, 2023). Besides, the flare QPPs are also modulated by the LRC-circuit oscillation, which needs

the current-carrying plasma loop (e.g., Tan et al. 2016; Li et al. 2020b). It appears that one mechanism could well trigger some certain flare QPPs, but it failed to drive all the observed QPPs, and the generation mechanism seems to be related to the observed period or the various wavebands (e.g., Kupriyanova et al. 2020).

Recently, the localizing QPPs were simultaneously observed in HXR and microwave emissions, but the measured quasi-periods were always shorter than 60 s (e.g., Kou et al. 2022; Collier et al. 2024; Shi et al. 2024). In this study, we localize the flare QPPs at a long period of about 200 s, which are simultaneously seen in wavelengths of HXR, microwave, and Ly α during an X-class flare. The article is organized as follows: Section 2 introduces the observations, Section 3 shows the data analysis and our main results, and Section 4 presents the conclusion and discussion.

2. Observations

We analyze an X6.4 flare that occurred in the active region of NOAA 13590 on 2024 February 22. It began at \sim 22:08 UT, reached its SXR maximum at \sim 22:34 UT, and ended at about \sim 22:43 UT¹. The X6.4 flare was simultaneously measured by the Hard X-ray Imager (HXI; Su et al. 2019; Zhang et al. 2019) and the Lyman-alpha Solar Telescope (LST; Chen et al. 2019; Feng et al. 2019) on board the Advanced Space-based Solar Observatory (ASO-S; Huang et al. 2019; Gan et al. 2023), the Spectrometer/Telescope for Imaging X-rays (STIX; Krucker et al. 2020) on Solar Orbiter, the Solar Upper Transition Region Imager (SUTRI; Bai et al. 2023), the Geostationary Operational Environmental Satellite (GOES), the Atmospheric Imaging Assembly (AIA; Lemen et al. 2012) and the Helioseismic and Magnetic Imager (HMI; Schou et al. 2012) aboard the Solar Dynamics Observatory (SDO), the Nobeyama Radio Polarimeters (NoRP), and the Expanded Owens Valley Solar Array (EOVSA; Gary et al. 2011).

HXI provides the HXR imaging spectroscopy of solar flares in the energy range of \sim 15–300 keV. The time cadence is 4 s in the regular mode and could be as high as 0.125 s in the flare mode. We use the data product at Level 1 (L1) in the HXR energy range of 20–300 keV, both the light curves and images are analyzed. STIX measures X-ray imaging spectroscopy in the energy range of 4–150 keV during solar flares. The data product of QL1 at 25–84 keV is used, which has a time cadence of 4 s. The advantage of this data type is that we can use it as early as possible since it releases quickly. GOES provides SXR light curves at 1–8 Å and 0.5–4 Å with a time cadence of 1 s. NoRP measures solar microwave fluxes at six frequencies with a time cadence of 1 s. EOVSA takes the solar radio dynamic spectrum in the frequency range of \sim 1–18 GHz, and its time cadence can be as high as 1 s, but some data gaps occasionally appear in the EOVSA spectrum.

AIA provides full-disk solar maps in EUV/UV wavebands, the time cadence of seven EUV wavebands is 12 s, and that of two UV wavebands is 24 s. In this study, we use AIA maps in seven

¹<https://www.solarmonitor.org/?date=20240223>

wavebands of 193 Å (~ 20 MK), 131 Å (~ 11 MK), 94 Å (~ 6.3 MK), 171 Å (~ 0.63 MK), 1600 Å (~ 0.1 MK), 304 Å (~ 0.05 MK), and 1700 Å (~ 0.005 MK). We want to state that the temperature in each waveband refers to the flare model. HMI takes the full-disk solar magnetogram, dopplergram, and continuum filtergram. We analyze the line-of-sight (LOS) magnetogram, which has a time cadence of 45 s. The AIA maps and HMI magnetogram have been pre-processed by “aia_prep.pro” and “hmi_prep.pro”, and thus they both have a pixel scale of $0.6''$. LST includes two telescopes, the Solar Disk Imager (SDI) takes the Ly α maps at 1216 Å, and the White-light Solar Telescope captures white-light maps at 3600 Å. Similar to HXI, the cadence of SDI is 60 s in the regular mode and changes to ~ 6 s in the burst mode. In this study, the SDI images in the regular mode is used, since the burst mode misses some data during the impulsive phase of the X-class flare. SUTRI takes full-disk solar maps at Ne VII 465 Å (Tian 2017). It has a time cadence of roughly 30 s and a pixel scale of $\sim 1.23''$. However, only a few maps are captured by SUTRI during the X6.4 flare, which is used to show the flare shape at 465 Å.

3. Data Analysis and Results

Figure 1 presents the full-disk light curves in wavelengths of SXR/HXR and microwave. Panel (a) shows the SXR fluxes recorded by GOES at 1–8 Å and 0.5–4 Å from 22:02 UT to 22:59 UT on 2024 February 22, which shows an X6.4-class flare and reaches its maximum at $\sim 22:34$ UT in GOES 1–8 Å, as indicated by the dashed vertical line. Panel (b) draws the HXR fluxes during 22:17–22:37 UT measured by ASO-S/HXI at 20–50 keV, 50–100 keV and its background (BKG), and 100–300 keV, as well as captured by STIX at 25–50 keV and 50–84 keV. Noting that STIX was located at 0.74 AU, and it was 26.5° from the Sun-Earth line in this event. One can immediately notice that three successive pulsating features simultaneously appear in the light curves of HXI 50–100 keV and STIX 50–84 keV between about 22:24 UT and 22:34 UT, as marked by the Arabic numerals ‘1’, ‘2’ and ‘3’. The three successive pulsations might be regarded as a candidate of flares QPPs in the HXR channel. Conversely, we do not find similar three pulsations in the HXR fluxes at HXI 20–50 keV and 100–300 keV, and STIX 25–50 keV. The light curves at HXI 20–50 keV and STIX 25–50 keV seem to reveal a group of pulses with a small amplitude, which is absolutely different from those three successive pulsations with a large amplitude. There is not any apparent signature in the light curve at HXI 100–300 keV, suggesting that the high-energy particles are rarely accelerated in the X6.4 flare. Panel (c) shows the microwave light curves and the EOVSa spectrogram. Similar to those HXR fluxes at HXI 50–100 keV and STIX 50–84 keV, these microwave fluxes in the high frequencies of NoRP 17 GHz and EOVSa 15.1 GHz also show three successive pulsations with a large amplitude during $\sim 22:24$ – $22:34$ UT, which could be considered as the QPP feature in the microwave emission. On the other hand, the microwave flux in the low microwave frequency of NoRP 3.75 GHz appears to show more than three pulsations, and their durations are obviously longer than those seen in the high microwave frequency. The radio dynamic spectrum in the frequency range of ~ 1 –18 GHz firmly confirms that the microwave radiation at the low frequency has longer pulses. So, we do not analyze the microwave flux at the

low frequency. It should be pointed out that the black vertical line in the EOVSa spectrogram is mainly due to the data gap.

In order to examine the periodicity of the flare QPP, we applied the wavelet transform method within a mother function of ‘Morlet’ (Torrence & Compo 1998), as shown in Figure 2. Here, the HXR light curve recorded by HXI is interpolated as a uniform cadence of 4 s. Panels (a1)–(a4) present the Morlet wavelet analysis results in the HXR channel. The raw light curves recorded by HXI 50–100 keV and STIX 50–84 keV appear to correlate remarkably well with each other, and their linear Pearson correlation coefficient (cc.) is about 0.93, as shown in panel (a1). Noting that the HXI flux at 50–100 keV has been removed its background emission, and the long-term trend at HXI 50–100 keV is calculated by a smoothing window of 6 minutes, as indicated by the dashed curve. The 6-minutes window is chosen because we want to suppress the long-period trend and enhance the short-period QPP, i.e., the quasi-period of 3–4 minutes (e.g., Yuan et al. 2019; Li et al. 2020a, 2022). Panel (a2) shows the detrended time series at HXI 50–100 keV, which is normalized to the maximum of its long-term trend. The detrended time series also reveals three successive pulsations, and they appear to a one-to-one correspondence with those pulsations in the raw HXR flux, confirming that the smoothing window can enhance the QPP feature. Moreover, the modulation depth of the QPP feature, which is regarded as the ratio between the oscillating amplitude and the maximum of its long-term trend, can reach roughly 210%. Then, the wavelet power and global wavelet power spectra of the detrended time series are shown in Figure 2 (a3) and (a4). They are mainly dominated by two bulks of power spectra inside the 99% significance level, implying the presence of double periods. The dominant periods are identified from the peak/center of the global wavelet power spectrum, and their uncertainties could be determined by the half full width at the 99% significance level. So, double periods of $\sim 200 \pm 40$ s and $\sim 95 \pm 10$ s are identified in the HXR channel.

Figure 2 (b1)–(b4) show the Morlet wavelet analysis results in the microwave emission. The raw light curves measured by NoRP 17 GHz and EOVSa 15.1 GHz agree well with each other, and their correlation coefficient is about 0.89, as shown in panel (b1). The overlaid dashed curve is the long-term trend with the same smoothing window of 6-minutes at NoRP 17 GHz. Panel (b2) draws the normalized detrended time series, as normalization by the maximum of its long-term trend. It shows similar three successive pulsations and the modulation depth of the QPP feature could be as high as 110%. Panels (b3) and (b4) present the wavelet power and global wavelet power spectra for the detrended time series at NoRP 17 GHz. Similar to what has been seen in the HXR channel, double periods within large uncertainties are determined from the global wavelet power spectrum, which are $\sim 200 \pm 50$ s and $\sim 95 \pm 10$ s.

To localize the generated source of these long-periodic pulsations, Figure 3 shows the multiple-wavelength images during the three pulsations. Panels (a1)–(a3) plot the UV maps with a field-of-view (FOV) of $\sim 200'' \times 200''$ in the wavelength of AIA 1700 Å at three time instances. It can be seen that the X6.4 flare is located near a sunspot and exhibits some bright features in those UV maps. The main body of the X6.4 flare consists of several kernel-like structures, and they form

a quasi-circular profile shape. A remote ribbon-like structure can be seen in the east of the main body. All those observational facts suggest that the X6.4 flare may be regarded as a circular-ribbon flare. The HXR source in the energy range of HXI 50–100 keV is overlaid on the brightest kernel, as outlined by the green contours, and the contour levels are set at 20% and 50%, respectively. Here, the HXR images during three pulsations are reconstructed by the HXL-CLEAN method, utilizing the detectors from D29 to D91, i.e., the subcollimator group G4 to G10. The fine grids of G1 to G3 are excluded, because they are not calibrated well and we do not focus on the fine structure (cf. Li et al. 2023). The gold box outlines an umbral region in the sunspot, which is used to integrate the umbral light curve. Figure 3 (b1)–(b3) show the EUV maps in the high-temperature channel of AIA 193 Å and 131 Å (blue contours). We can see that the X6.4 flare shows several loop-like structures that connect those kernel-like structures seen in AIA 1700 Å maps, it also shows a remote loop-like feature. The black rectangle outlines the flare area used to integrate the local light curves. Panels (c) and (d) present the EUV and Ly α maps in wavelengths of SUTRI 465 Å, AIA 304 Å (cyan contours), and SDI 1216 Å (yellow contours), and their formation temperature are much lower than that in AIA 193 Å and 131 Å. They manifested as a main circular profile shape and a remote ribbon structure, which can be used to co-align those maps measured by various instruments, as indicated by the cyan and yellow contours. Figure 3 (e) shows the LOS magnetogram observed by HMI, and it shows that the main circular-ribbon feature is located in positive and negative magnetic fields, which formed a quasi-circular shape, while the remote ribbon appears in the negative magnetic field. All those imaging observations suggest that the X6.4 flare is a circular-ribbon flare with a fan-spine topology, which is produced in the complicated magnetic structure.

Figure 4 (a) presents the local light curves integrated over the flare area in multi-wavelengths measured by SDO/AIA and ASO-S/LST/SDI. In this study, the time cadence of SDO/AIA is chosen as 24 s for all AIA maps to avoid imaging saturation (cf. Li et al. 2015). These light curves are used as normalization, i.e., $\frac{I-I_{\min}}{I_{\max}-I_{\min}}$, where I represents the measured intensity, I_{\min} and I_{\max} are the minimum and maximum intensities. Similar to what has been seen in the HXR and microwave fluxes, the UV/EUV and Ly α light curves at low-temperature channels (e.g., AIA 1700 Å, 1600 Å and 304 Å, SDI 1216 Å) appear for three successive pulsations during $\sim 22:24$ – $22:34$ UT, suggesting the presence of flare QPPs with a quasi-period of roughly 200 s. On the other hand, the EUV light curves at high-temperature channels (e.g., AIA 193 Å, 131 Å, 94 Å) do not show any signature of the QPP feature with the same period. It is interesting that the peak time of the high-temperature channels is later and later with a decrease in the formation temperature, as indicated by the vertical short lines, suggesting that the hot flare loops are cooling with time. We also calculate the linear Pearson correlation coefficients (cc.) of these light curves, and they are all relative to the light curve at AIA 1700 Å. Obviously, the correlation coefficients of those light curves in the low-temperature channels are all larger than 0.9, while those in the high-temperature channels are a bit small, i.e., ≤ 0.55 . These observational facts confirm that the QPP feature could only be seen in the low-temperature channels.

We note that the X6.4 flare is located on the edge of a sunspot, and the quasi-period of the flare

QPP is roughly equal to 3 minutes. Therefore, we also plot the local light curves integrated over the umbral region in the neighboring sunspot at AIA 1700 Å and 1600 Å, as shown in Figure 4 (b). Similar to those flare fluxes, they both show three successive pulsations, as marked by the arabic numerals, suggesting the presence of similar periods. Moreover, they have high correlations with the flare light curve at AIA 1700 Å, i.e., their correlation coefficient could be as high as 0.90/0.93. At last, the normalized magnetic fluxes integrated over the flare area are given in panel (c), including the total, positive, and negative magnetic fluxes. It can be seen that both the positive and negative magnetic fluxes appear to decrease when the start of flare QPPs, as indicated by the gold arrow. The total magnetic flux reveals a significant reduction, indicating a process of magnetic cancellation. These observations imply the occurrence of magnetic reconnection during the flare QPPs. However, we do not see similar three pulsations in the time series of magnetic fluxes, which might be due to the lower sensitivity and time resolution of SDO/HMI.

Figure 5 shows the Morlet wavelet analysis results in the wavelength of AIA 1700 Å at the flare area (a1–a4) and the umbral region (b1–b4), respectively. Using the same smoothing window of 6 minutes, the raw light curve is decomposed into the long-term trend (dashed lines) and the detrended time series (a2 and b2). We should state that the raw light curves are normalized to their maximum intensity, and the detrended time series are normalized to the maximum of their long-term trends. Thus, we can estimate the modulation depth of the QPP feature, which is identified as the ratio between the oscillating amplitude and the maximum of its long-term trend. The modulation depth is about 6%–8%, which is much lower than that observed in the HXR/microwave emission. The quasi-periods can be determined from the wavelet power or global wavelet power spectra, which are estimated to be $\sim 205 \pm 25$ s in the flare area, and $\sim 205 \pm 20$ s in the umbral region, as shown in panels (a4) and (b4). Here, the short period at about 95 s is not detected, which is different from what has been observed in the HXR/microwave channel.

In order to offer much more insight in the structure of magnetic fields above the targeted active region, two maps showing the active region of NOAA 13590 before the initiation of the X6.4 flare are drawn in Figure 6. Panel (a) presents the EUV map at 22:00:09 UT in the wavelength of AIA 171 Å, and it clearly shows a number of coronal loops in the targeted active region. The over-plotted blue and red contours represent the polarity magnetic fields measured by SDO/HMI before the onset of the the X6.4 flare, and the green contours indicate the core area of the X6.4 flare observed by ASO-S/HXI. It can be seen that the interested sunspot was dominated by a strong positive magnetic field, as outlined by the large blue contour. And the sunspot is located below some coronal fan-like structures. The flare core and the coronal fan above the sunspot are connected by a loop system, as indicated by the turquoise arrow. Figure 6 (b) shows the magnetic field topology on the flaring active region, which is derived from the potential field source surface (PFSS) extrapolation (Schrijver & De Rosa 2003) based on the synoptic HMI magnetogram. The flaring active region is mainly dominated by a large number of closed magnetic field lines, while the open magnetic field line only accounts for a small portion, as marked by the white and purple lines. We also notice that the flare area and the sunspot are connected by some closed field lines,

as indicated by the turquoise arrow. Both the EUV map at AIA 171 Å and the PFSS extrapolated result suggest that the X6.4 flare and the sunspot are mutually influenced via some magnetic loops.

4. Conclusion and Discussion

By using the combined HXR, microwave, $\text{Ly}\alpha$, and UV/EUV observations from HXI, STIX, EOVSA, NoRP, LST, SUTRI, HMI, and AIA, we investigate the long-periodic pulsations during the impulsive phase of an X6.4 flare and localize their source locations through reconstructing the HXR map at HXI 50–100 keV. Double periods are determined by the Morlet wavelet transform technique in HXR and microwave wavebands. We also explore the generation mechanism of flare QPPs, which could be related to the umbral oscillation in the neighboring sunspot, because the quasi-period of flare QPPs matches the periodicity of umbral oscillations in the nearby sunspot.

In our case, three successive pulsations are simultaneously observed in HXR, microwave, $\text{Ly}\alpha$, UV, and low-temperature EUV wavelengths, which could be regarded as flare QPPs. The wavelet analysis results suggest that the dominant period of the flare QPP is ~ 200 s, and the period uncertainties are varied in different wavelengths. The flare QPPs at long quasi-periods are frequently detected in wavelengths of $\text{Ly}\alpha$, UV/EUV, and SXR (e.g., Kumar et al. 2015; Tan et al. 2016; Milligan et al. 2017; Li 2022). However, such long-period QPP are rarely localized in HXR and microwave emissions. Based on the observation from EOVSA, the flare QPPs with varying periods of ~ 10 – 20 s and ~ 30 – 60 s were seen in the microwave emission (cf. Kou et al. 2022). Combined the observations from STIX and EOVSA, the flare QPPs with fast variations on timescales evolving from ~ 7 s to ~ 35 s were found in HXR and microwave channels (cf. Collier et al. 2024). Using the observations from HXI, STIX, and the Chashan Broadband Solar millimeter spectrometer, the flare QPP with a period of ~ 27 s is simultaneously found in HXR and microwave channels (Shi et al. 2024). Obviously, those quasi-periods are much shorter than that is observed in our case, although they localised and imaged the flare QPPs in HXR or microwave channels. On the other hand, the flare QPPs at the quasi-period of about 4 minutes were simultaneously detected in wavebands of HXR and low-frequency radio emissions, but they identified the source locations of flare QPPs by using the imaging observations at UV/EUV wavelengths (e.g., Li et al. 2015). Kumar et al. (2016) reported the 3-minutes QPPs and determined their source region by using the HXR and microwave observations, and the 3-minutes period could be simultaneously found in the HXR 25–50 keV, microwave frequencies of 2 GHz, 3.75 GHz, 9.4 GHz, and 17 GHz, as well as metric and decimetric radio frequencies of 25–180 MHz, 245 MHz, and 610 MHz. Here, the long-periodic pulsations at periods of ~ 200 s can be observed in the HXR channel above 50 keV, microwave frequencies above 10 GHz, but they can not be seen at HXR wavebands below 50 keV and radio frequencies below 10 GHz. Interestingly, the long-periodic pulsations can also be detected in the wavelengths of $\text{Ly}\alpha$, UV and low-temperature EUV. The modulation depth of long-periodic pulsations, which is defined as the ratio between the pulsation amplitude and the maximum of its long-term trend, is extremely large in HXR and microwave channels. For instance, it can reach 210% in the HXR channel and

could be as high as 110% in the high-frequency microwave emission. They are much larger than the modulation depth in wavelengths of UV/EUV and $\text{Ly}\alpha$, i.e., $\leq 8\%$. Our results in HXR and microwaves are much bigger than previous findings, i.e., the modulation depth of $\sim 20\%–25\%$ in HXR, γ -rays, and microwave emission (e.g., Nakariakov et al. 2010; Li & Chen 2022). Thus, the long-periodic pulsations seen in the HXR and microwave channels show an extremely-large modulation depth. This feature is reasonable. Because the solar radiation in HXR and γ -rays are mainly from the flare area, their background emission is quite weak, and the modulation depth could be large. Conversely, the solar radiation in SXR and UV/EUV can be from the entire Sun, regardless of whether there is a flare occurring or not, so their background emission is strong, resulting in the small-amplitude oscillation (e.g., Simões et al. 2015; Ning 2017; Dominique et al. 2018; Li et al. 2020c; Shi et al. 2024).

Until now, the generation mechanism of flare QPPs is still not fully understood (Kupriyanova et al. 2020; Zimovets et al. 2021a). The long-periodic pulsations are simultaneously observed in wavebands of HXR, microwave, $\text{Ly}\alpha$, UV and low-temperature EUV during the flare impulsive phase. Moreover, the magnetic cancellation occurs when the onset of flare QPPs. Thus, they could be generated by nonthermal electrons that are periodically accelerated by repetitive magnetic reconnections (Yuan et al. 2019; Clarke et al. 2021; Li et al. 2023). The HXR images show that the source locations of these long-periodic pulsations are nearly not moving over time, indicating that the repetitive magnetic reconnections are not slipping (Li & Zhang 2015). Now the question is whether the periodic reconnection is spontaneous or induced? Considering the large uncertainty, the quasi-period of ~ 200 s is close to that of ~ 3 minutes in the sunspot, particularly the umbral oscillation in the chromosphere (e.g., Sych et al. 2009; Kumar et al. 2016; Li et al. 2020d; Wang et al. 2024). By checking the imaging observations captured by HXI and AIA, we find that the X6.4 flare is located at the edge of a sunspot. Then, a small umbral region in the sunspot is chosen to look at its periodicity. Similar to the flare area, the time series at the umbral region reveals a similar quasi-period. Therefore, the long-periodic pulsations could be associated with the umbral oscillation at the neighboring sunspot, that is, it is triggered by the slow magnetoacoustic wave leaking from the sunspot umbra in the photosphere, and then propagates upwardly to the chromosphere and corona (cf. Yuan et al. 2011). Both the AIA 171 Å map and the PFSS extrapolation have demonstrated that the flare core and the sunspot are linked by some magnetic field lines, implying that the slow magnetoacoustic wave could propagate from the coronal plasma fan above the sunspot to the flare area along the magnetic loop (Meadowcroft et al. 2024). Briefly, the quasi-periodicity of magnetic reconnection during the X6.4 flare is most likely to be induced by the slow magnetoacoustic wave originating from the sunspot umbra, and it further modulates the flare QPPs in wavelengths of HXR, microwave, $\text{Ly}\alpha$, UV and low-temperature EUV during the impulsive phase (Clarke et al. 2021; Zimovets et al. 2021b; Li & Chen 2022).

Another interesting point is that double periods are nearly simultaneously observed in wavebands of HXR and microwave during the impulsive phase of the X6.4 flare. The long period peaked at ~ 200 s is simultaneously seen in wavelengths of HXI 50–100 keV, STIX 50–84 keV,

EOVSA 15.1 GHz, NoRP 17 GHz, SDI 1216 Å, AIA 1600 Å, 1700 Å, and 304 Å, while the short period centered at ~ 95 s can be only found in HXR and microwave channels during the flare impulsive phase. The short period is not observed in Ly α and UV wavelengths, largely due to the low time resolution of LST/SDI and SDO/AIA. The ratio of double periods are roughly equal to 2.1, which is consistent with previous observations about the flare QPPs within double periods (e.g., Inglis & Nakariakov 2009; Lu et al. 2021; Li 2022). Our observational result agrees with the theoretical expectation of the fundamental and harmonic modes of weakly dispersive MHD waves (Nakariakov & Verwichte 2005). So, the long period is regarded as the fundamental mode of the slow magnetoacoustic wave that originated from the umbral oscillation in the nearby sunspot, and the short period could be considered as its second-harmonic mode.

This work is supported by the National Key R&D Program of China 2022YFF0503002 (2022YFF0503000), NSFC under grants 12333010 and 12073081, and the Strategic Priority Research Program of the Chinese Academy of Sciences, grant No. XDB0560000. D. Li is also supported by the Surface Project of Jiangsu Province (BK20211402) and Yunnan Key Laboratory of Solar Physics and Space Science under the number of YNSPCC202207. We thank the teams of ASO-S, SUTRI, GOES, SDO, NoRP, and EOVSA for their open data use policy. ASO-S mission is supported by the Strategic Priority Research Program on Space Science, the Chinese Academy of Sciences, Grant No. XDA15320000. SUTRI is a collaborative project conducted by the National Astronomical Observatories of CAS, Peking University, Tongji University, Xi'an Institute of Optics and Precision Mechanics of CAS and the Innovation Academy for Microsatellites of CAS. SDO is NASA's first mission in the Living with a Star program. The STIX instrument is an international collaboration between Switzerland, Poland, France, Czech Republic, Germany, Austria, Ireland, and Italy.

REFERENCES

- Altyntsev, A. T., Meshalkina, N. S., Sych, R. A., et al. 2022, *A&A*, 663, A149. doi:10.1051/0004-6361/202243144
- Bai, X., Tian, H., Deng, Y., et al. 2023, *Research in Astronomy and Astrophysics*, 23, 065014. doi:10.1088/1674-4527/accc74
- Clarke, B. P., Hayes, L. A., Gallagher, P. T., et al. 2021, *ApJ*, 910, 123. doi:10.3847/1538-4357/abe463
- Chen, B., Li, H., Song, K.-F., et al. 2019, *Research in Astronomy and Astrophysics*, 19, 159. doi:10.1088/1674-4527/19/11/159
- Collier, H., Hayes, L. A., Yu, S., et al. 2024, *A&A*, 684, A215. doi:10.1051/0004-6361/202348652
- Corchado Albelo, M. F., Kazachenko, M. D., & Lynch, B. J. 2024, *ApJ*, 965, 16. doi:10.3847/1538-4357/ad25f4

- Dennis, B. R., Tolbert, A. K., Inglis, A., et al. 2017, *ApJ*, 836, 84. doi:10.3847/1538-4357/836/1/84
- Dominique, M., Zhukov, A. N., Dolla, L., et al. 2018, *Sol. Phys.*, 293, 61. doi:10.1007/s11207-018-1281-x
- Feng, L., Li, H., Chen, B., et al. 2019, *Research in Astronomy and Astrophysics*, 19, 162. doi:10.1088/1674-4527/19/11/162
- Gan, W., Zhu, C., Deng, Y., et al. 2023, *Sol. Phys.*, 298, 68. doi:10.1007/s11207-023-02166-x
- Gary, D. E., Hurford, G. J., Nita, G. M., et al. 2011, *AAS/Solar Physics Division Abstracts #42*
- Huang, Y., Li, H., Gan, W.-Q., et al. 2019, *Research in Astronomy and Astrophysics*, 19, 164. doi:10.1088/1674-4527/19/11/164
- Inglis, A. R. & Nakariakov, V. M. 2009, *A&A*, 493, 259. doi:10.1051/0004-6361/200810473
- Inglis, A., Hayes, L., Guidoni, S., et al. 2023, *BAAS*. doi:10.3847/25c2cfef.55d6b861
- Kashapova, L. K., Kupriyanova, E. G., Xu, Z., et al. 2020, *A&A*, 642, A195. doi:10.1051/0004-6361/201833947
- Karlický, M. & Rybák, J. 2020, *ApJS*, 250, 31. doi:10.3847/1538-4365/abb19f
- Karampelas, K., McLaughlin, J. A., Botha, G. J. J., et al. 2022, *ApJ*, 925, 195. doi:10.3847/1538-4357/ac3b53
- Kou, Y., Cheng, X., Wang, Y., et al. 2022, *Nature Communications*, 13, 7680. doi:10.1038/s41467-022-35377-0
- Krucker, S., Hurford, G. J., Grimm, O., et al. 2020, *A&A*, 642, A15. doi:10.1051/0004-6361/201937362
- Kumar, P., Nakariakov, V. M., & Cho, K.-S. 2015, *ApJ*, 804, 4. doi:10.1088/0004-637X/804/1/4
- Kumar, P., Nakariakov, V. M., & Cho, K.-S. 2016, *ApJ*, 822, 7. doi:10.3847/0004-637X/822/1/7
- Kupriyanova, E., Kolotkov, D., Nakariakov, V., et al. 2020, *Solar-Terrestrial Physics*, 6, 3. doi:10.12737/stp-61202001
- Lemen, J. R., Title, A. M., Akin, D. J., et al. 2012, *Sol. Phys.*, 275, 17. doi:10.1007/s11207-011-9776-8
- Li, B., Antolin, P., Guo, M.-Z., et al. 2020, *Space Sci. Rev.*, 216, 136. doi:10.1007/s11214-020-00761-z
- Li, D., Ning, Z. J., & Zhang, Q. M. 2015, *ApJ*, 807, 72. doi:10.1088/0004-637X/807/1/72

- Li, D., Kolotkov, D. Y., Nakariakov, V. M., et al. 2020a, *ApJ*, 888, 53. doi:10.3847/1538-4357/ab5e86
- Li, D., Li, Y., Lu, L., et al. 2020b, *ApJ*, 893, L17. doi:10.3847/2041-8213/ab830c
- Li, D., Lu, L., Ning, Z., et al. 2020c, *ApJ*, 893, 7. doi:10.3847/1538-4357/ab7cd1
- Li, D., Yang, X., Bai, X. Y., et al. 2020d, *A&A*, 642, A231. doi:10.1051/0004-6361/202039007
- Li, D., Ge, M., Dominique, M., et al. 2021b, *ApJ*, 921, 179. doi:10.3847/1538-4357/ac1c05
- Li, D. & Chen, W. 2022, *ApJ*, 931, L28. doi:10.3847/2041-8213/ac6fd2
- Li, D., Shi, F., Zhao, H., et al. 2022, *Frontiers in Astronomy and Space Sciences*, 9, 1032099. doi:10.3389/fspas.2022.1032099
- Li, D. 2022, *Science in China E: Technological Sciences*, 65, 139. doi:10.1007/s11431-020-1771-7
- Li, D., Li, Z., Shi, F., et al. 2023, *A&A*, 680, L15. doi:10.1051/0004-6361/202348075
- Li, T. & Zhang, J. 2015, *ApJ*, 804, L8. doi:10.1088/2041-8205/804/1/L8
- Lu, L., Li, D., Ning, Z., et al. 2021, *Sol. Phys.*, 296, 130. doi:10.1007/s11207-021-01876-4
- Luo, Y., Chen, B., Yu, S., et al. 2022, *ApJ*, 940, 137. doi:10.3847/1538-4357/ac997a
- McLaughlin, J. A., De Moortel, I., Hood, A. W., et al. 2009, *A&A*, 493, 227. doi:10.1051/0004-6361:200810465
- Mehta, T., Broomhall, A.-M., & Hayes, L. A. 2023, *MNRAS*, 523, 3689. doi:10.1093/mnras/stad1619
- Meadowcroft, R. L., Zhong, S., Kolotkov, D. Y., et al. 2024, *MNRAS*, 527, 5302. doi:10.1093/mnras/stad3506
- Milligan, R. O., Fleck, B., Ireland, J., et al. 2017, *ApJ*, 848, L8. doi:10.3847/2041-8213/aa8f3a
- Millar, D. C. L., Fletcher, L., & Joshi, J. 2024, *MNRAS*, 527, 5916. doi:10.1093/mnras/stad3386
- Motyk, I. D., Kashapova, L. K., Setov, A. G., et al. 2023, *Geomagnetism and Aeronomy*, 63, 1062. doi:10.1134/S0016793223070174
- Nakariakov, V. M. & Verwichte, E. 2005, *Living Reviews in Solar Physics*, 2, 3. doi:10.12942/lrsp-2005-3
- Nakariakov, V. M., Foullon, C., Myagkova, I. N., et al. 2010, *ApJ*, 708, L47. doi:10.1088/2041-8205/708/1/L47

- Nakariakov, V. M., Anfinogentov, S., Storozhenko, A. A., et al. 2018, *ApJ*, 859, 154. doi:10.3847/1538-4357/aabfb9
- Nakariakov, V. M., Kolotkov, D. Y., Kupriyanova, E. G., et al. 2019, *Plasma Physics and Controlled Fusion*, 61, 014024. doi:10.1088/1361-6587/aad97c
- Nakariakov, V. M., Anfinogentov, S. A., Antolin, P., et al. 2021, *Space Sci. Rev.*, 217, 73. doi:10.1007/s11214-021-00847-2
- Ning, Z. 2017, *Sol. Phys.*, 292, 11. doi:10.1007/s11207-016-1037-4
- Ning, Z., Wang, Y., Hong, Z., et al. 2022, *Sol. Phys.*, 297, 2. doi:10.1007/s11207-021-01935-w
- Parks, G. K. & Winckler, J. R. 1969, *ApJ*, 155, L117. doi:10.1086/180315
- Schou, J., Scherrer, P. H., Bush, R. I., et al. 2012, *Sol. Phys.*, 275, 229. doi:10.1007/s11207-011-9842-2
- Schrijver, C. J. & De Rosa, M. L. 2003, *Sol. Phys.*, 212, 165. doi:10.1023/A:1022908504100
- Shi, F., Li, D., Ning, Z., et al. 2024, *Sol. Phys.*, 299, 30. doi:10.1007/s11207-024-02272-4
- Shen, Y., Yao, S., Tang, Z., et al. 2022, *A&A*, 665, A51. doi:10.1051/0004-6361/202243924
- Simões, P. J. A., Hudson, H. S., & Fletcher, L. 2015, *Sol. Phys.*, 290, 3625. doi:10.1007/s11207-015-0691-2
- Su, Y., Liu, W., Li, Y.-P., et al. 2019, *Research in Astronomy and Astrophysics*, 19, 163. doi:10.1088/1674-4527/19/11/163
- Sych, R., Nakariakov, V. M., Karlicky, M., et al. 2009, *A&A*, 505, 791. doi:10.1051/0004-6361/200912132
- Tan, B., Zhang, Y., Tan, C., et al. 2010, *ApJ*, 723, 25. doi:10.1088/0004-637X/723/1/25
- Tan, B., Yu, Z., Huang, J., et al. 2016, *ApJ*, 833, 206. doi:10.3847/1538-4357/833/2/206
- Takasao, S. & Shibata, K. 2016, *ApJ*, 823, 150. doi:10.3847/0004-637X/823/2/150
- Tian, H. 2017, *Research in Astronomy and Astrophysics*, 17, 110. doi:10.1088/1674-4527/17/11/110
- Torrence, C. & Compo, G. P. 1998, *Bulletin of the American Meteorological Society*, 79, 61. doi:10.1175/1520-0477(1998)079<0061:APGTWA>2.0.CO;2
- Thurgood, J. O., Pontin, D. I., & McLaughlin, J. A. 2017, *ApJ*, 844, 2. doi:10.3847/1538-4357/aa79fa
- Török, T., Aulanier, G., Schmieder, B., et al. 2009, *ApJ*, 704, 485. doi:10.1088/0004-637X/704/1/485

- Wang, T., Ofman, L., Yuan, D., et al. 2021, *Space Sci. Rev.*, 217, 34. doi:10.1007/s11214-021-00811-0
- Wang, Y., Fletcher, L., Mulay, S., et al. 2024, *ApJ*, 961, 231. doi:10.3847/1538-4357/ad10a9
- Xu, J., Ning, Z., Li, D., et al. 2023, *Universe*, 9, 215. doi:10.3390/universe9050215
- Yu, S., Chen, B., Sharma, R., et al. 2024, *Nature Astronomy*, 8, 50. doi:10.1038/s41550-023-02122-6
- Yuan, D., Nakariakov, V. M., Chorley, N., et al. 2011, *A&A*, 533, A116. doi:10.1051/0004-6361/201116933
- Yuan, D., Feng, S., Li, D., et al. 2019, *ApJ*, 886, L25. doi:10.3847/2041-8213/ab5648
- Zhao, H.-S., Li, D., Xiong, S.-L., et al. 2023, *Science China Physics, Mechanics, and Astronomy*, 66, 259611. doi:10.1007/s11433-022-2064-6
- Zhang, Z., Chen, D.-Y., Wu, J., et al. 2019, *Research in Astronomy and Astrophysics*, 19, 160. doi:10.1088/1674-4527/19/11/160
- Zhang, Q. 2024, *Reviews of Modern Plasma Physics*, 8, 7. doi:10.1007/s41614-024-00144-9
- Zhou, X., Shen, Y., Yuan, D., et al. 2024, *Nature Communications*, 15, 3281. doi:10.1038/s41467-024-46846-z
- Zimovets, I. V., McLaughlin, J. A., Srivastava, A. K., et al. 2021a, *Space Sci. Rev.*, 217, 66. doi:10.1007/s11214-021-00840-9
- Zimovets, I., Sharykin, I., & Myshyakov, I. 2021b, *Sol. Phys.*, 296, 188. doi:10.1007/s11207-021-01936-9

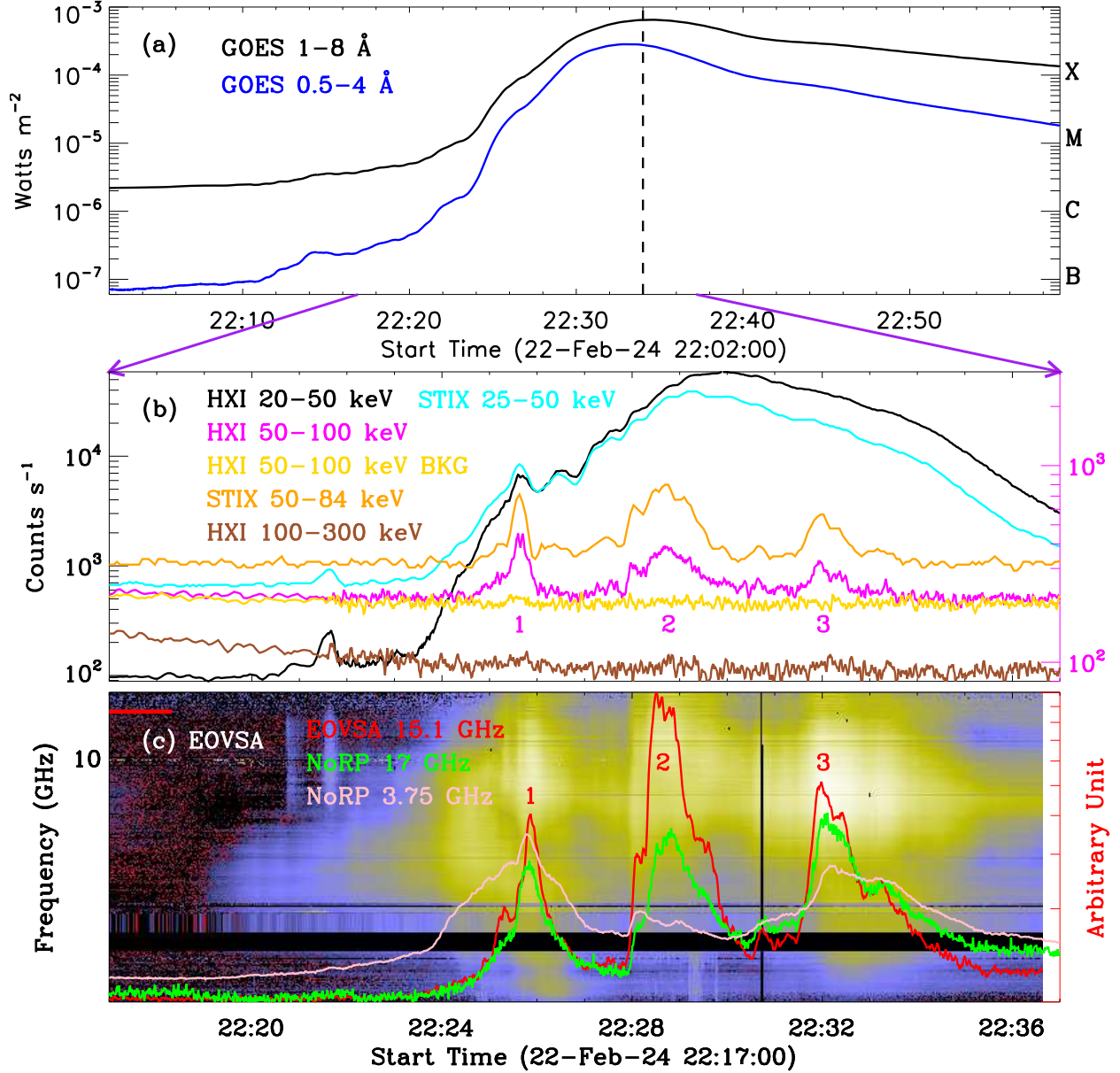


Fig. 1.— Full-disk light curves of the X6.4 flare on 2024 February 2. (a) SXR light curves measured by GOES 1–8 Å (black) and 0.5–4 Å (blue). The vertical dashed line indicates the peak time at GOES 1–8 Å. (b) HXR fluxes recorded by HXI 20–50 keV (black), 50–100 keV (magenta) and its background (gold), and 100–300 keV (brown), as well as STIX 25–50 keV (cyan) and 50–84 keV (orange). (c) Microwave fluxes captured by EOVSA 15.1 GHz (red), and NoRP 17 GHz (green) and 3.75 GHz (pink). The context image is the radio dynamic spectrum observed by EOVSA.

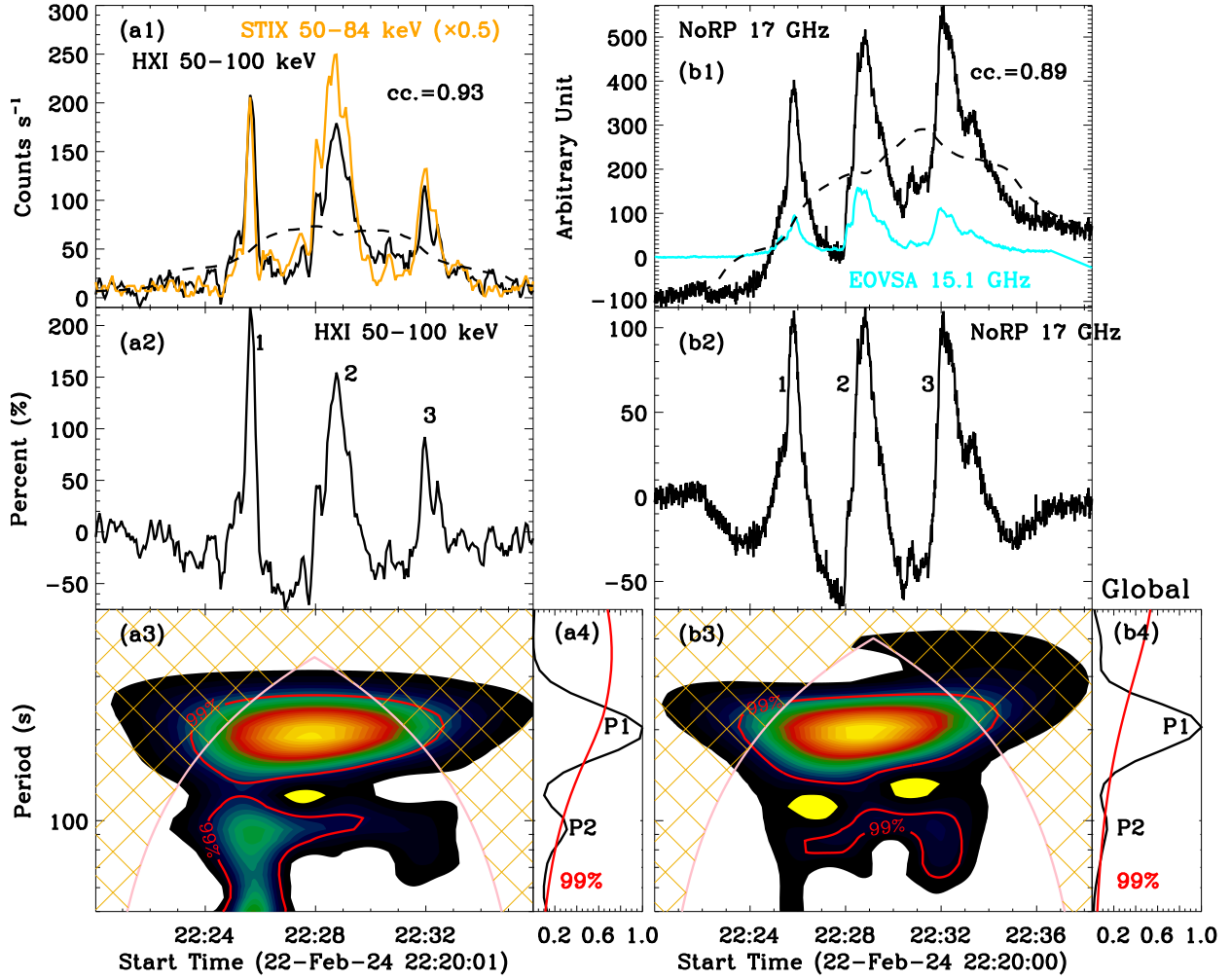


Fig. 2.— Morlet wavelet analysis results for the HXR and microwave light curves. (a1) & (b1) HXR and microwave fluxes recorded by HXI 50–100 keV, STIX 50–84 keV, NoRP 17 GHz, and EOVSVA 15.1 GHz, respectively. Here, the HXI flux has been subtracted from its background emission. The overlaid dashed lines represent long-term trends at HXI 50–100 keV and NoRP 17 GHz. (a2) & (b2) Detrended light curves normalized to their maximum of long-term trends in wavelengths of HXI 50–100 keV and NoRP 17 GHz. (a3) & (b3) Morlet wavelet power spectra. (a4) & (b4) Global wavelet power. The red contours or lines represent the significance level of 99%.

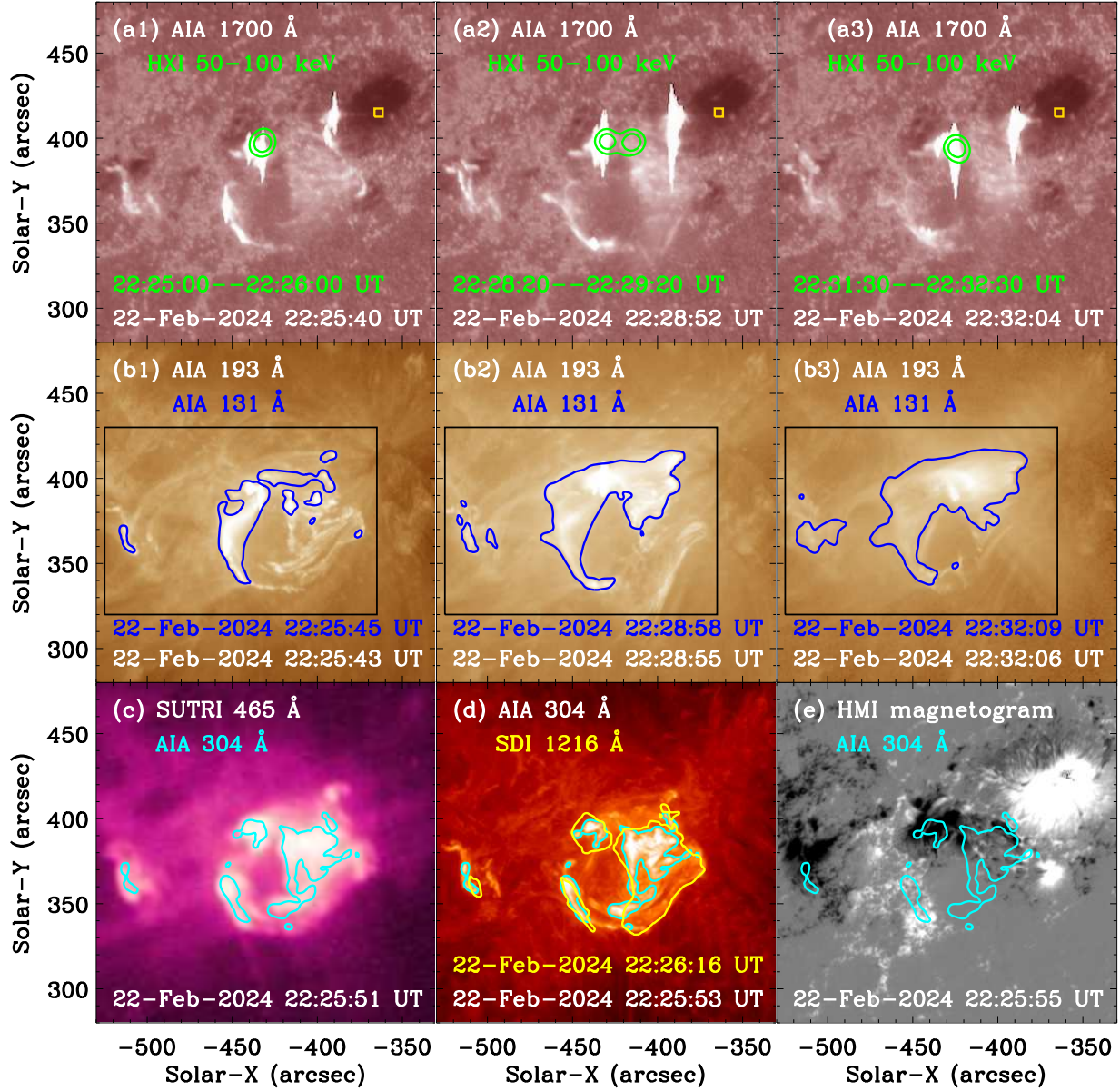


Fig. 3.— Multi-wavelength snapshots with a FOV of $\sim 200'' \times 200''$ during the X6.4 flare. (a1)–(a3) UV maps measured by AIA 1700 Å. The green contours represent the HXR radiation observed by ASO-S/HXI at 50–100 keV, and the levels are set at 20% and 50%, respectively. The gold box outlines an umbral region, which is applied to integrate over the umbral light curve. (b1)–(b3) EUV maps measured by AIA 193 Å, and the blue contours are the AIA 131 Å emissions. The black rectangle outlines the flare area used to integrate over the flare fluxes. (c) & (d) EUV maps captured by SUTRI 465 Å and AIA 304 Å. The cyan and yellow contours are the EUV emissions at AIA 304 Å and SDI 1216 Å, respectively. (e) HMI LOS magnetogram with a strength scale of ± 800 G.

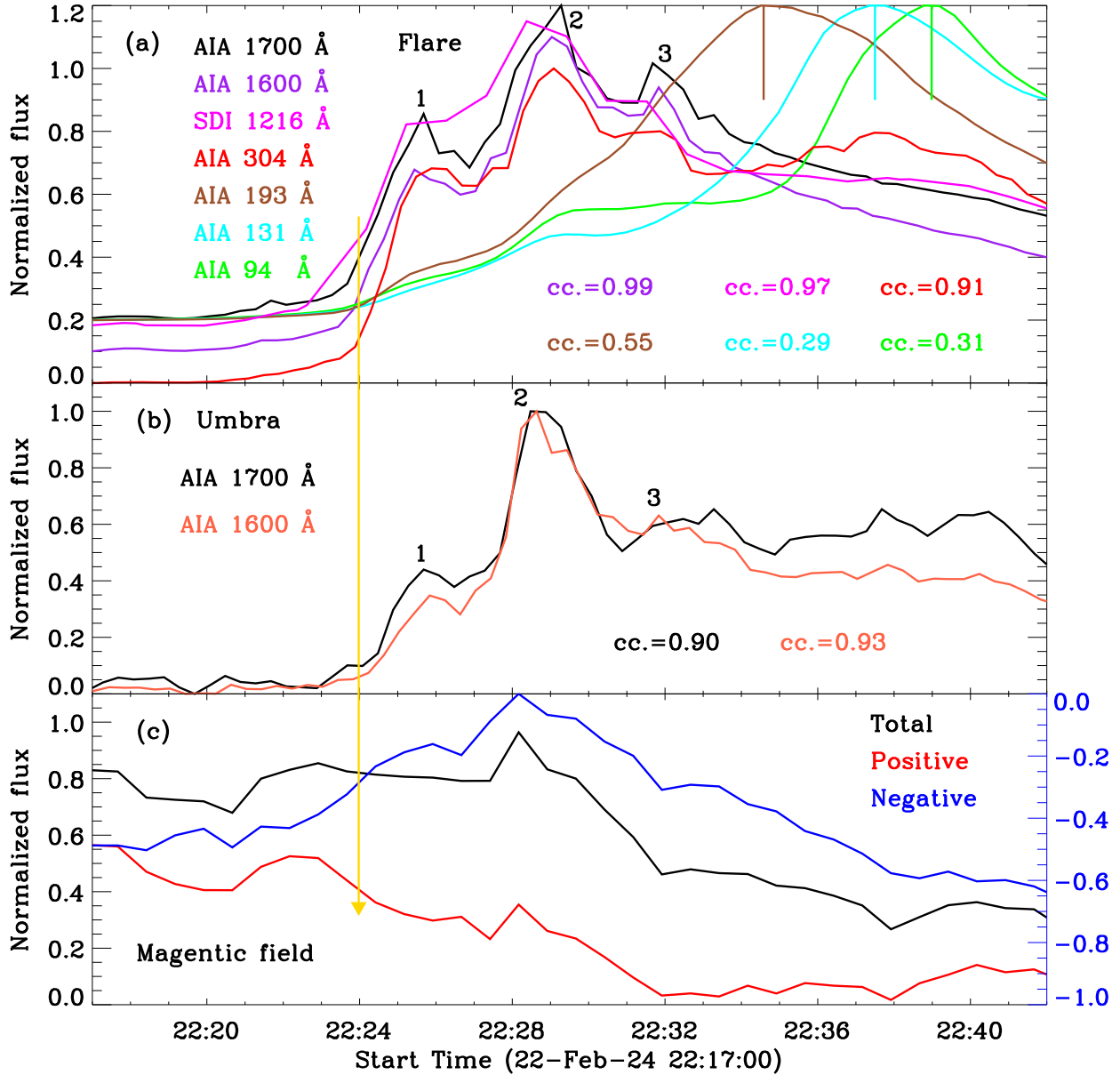


Fig. 4.— Local light curves during the X6.4 flare. (a) UV/EUV and $\text{Ly}\alpha$ fluxes integrated over the flare area in wavelengths of AIA 1700 Å (black), 1600 Å (purple), 304 Å (red), 193 Å (brown), 131 Å (cyan), and 94 Å (green), and SDI 1216 Å (magenta). The numbers mark three pulsations in the low-temperature channels, and the vertical short lines indicate the peak time of the high-temperature channels. (b) UV light curves integrated over the umbral region in wavelengths of AIA 1700 Å (black) and 1600 Å (tomato). (c) Time series of the magnetic flux integrated over the flare area for the total, positive, and negative magnetic fields, respectively. The gold arrow outlines the onset time of flare QPPs and the magnetic cancellation.

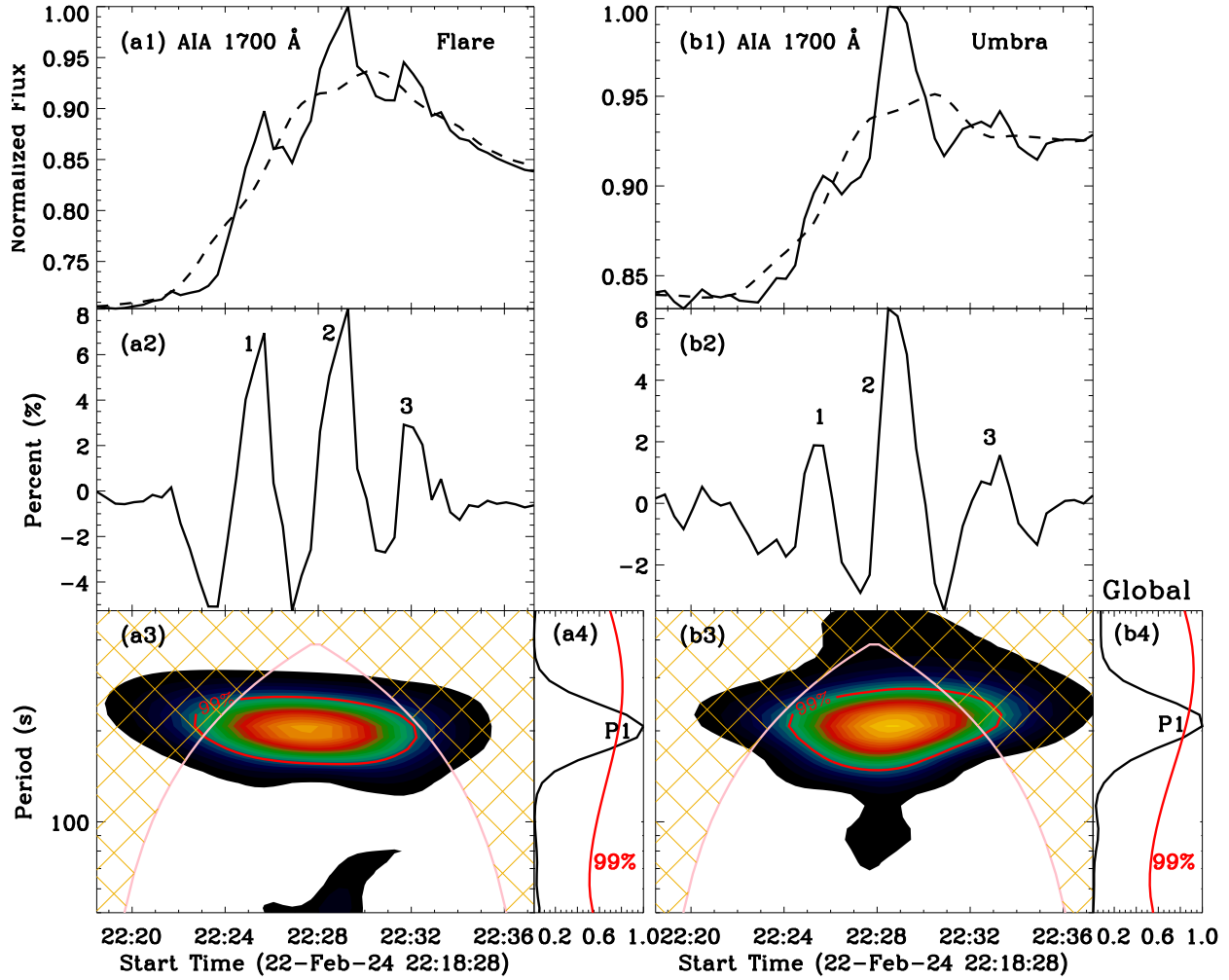


Fig. 5.— Similar to Fig. 2 but the wavelet analysis is performed for the AIA 1700 Å light curves integrated over the flare area (a1–a4) and the adjacent sunspot umbra (b1–b4), respectively.

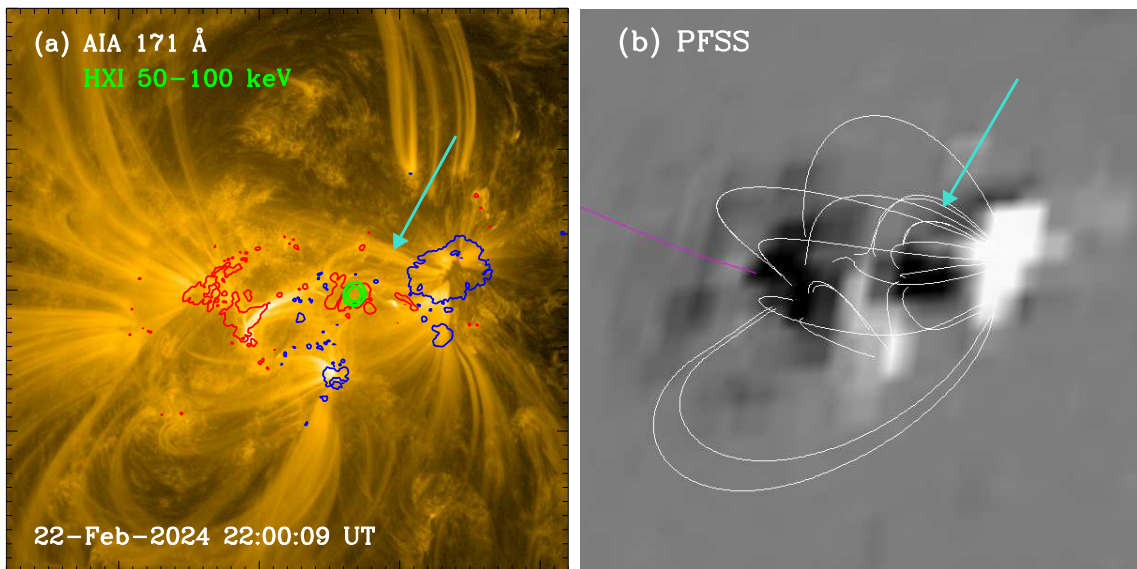


Fig. 6.— The active region of NOAA 13590 before the initiation of the X6.4 flare. (a) The EUV snapshot at AIA 171 Å. The blue and red contours are the positive and negative magnetic fields at the strength scale of ± 500 G, respectively. (b) The magnetic configuration derived from a PFSS model. The white and purple lines represent the closed and open magnetic fields. The turquoise arrow indicates some coronal loops or magnetic field lines that connect the flare core (green contours) and the sunspot.